Pirineos. Revista de Ecología de Montaña
Vol. 175
Jaca, Enero-Diciembre, 2020, e051
ISSN-l: 0373-2568
https://doi.org/10.3989/pirineos.2020.175001

SPATIO-TEMPORAL PATTERNS OF LANDSLIDES AND EROSION IN TROPICAL ANDEAN CATCHMENTS

Distribución espacio-temporal de los deslizamientos y erosión hídrica en una cuenca Andina tropical

Veerle Vanacker[1]*, Marie Guns[1], Francois Clapuyt[1], Vincent Balthazar[1], Gustavo Tenorio[2-4], Armando Molina[3-4].

[1] Earth and Life Institute, George Lemaître Center for Earth and Climate Research,
Université Catholique de Louvain, L4.03.08, Louvain-la-Neuve, 1348, Belgium.
[2] Facultad de Ciencias Agropecuarias, Campus Yanuncay, Universidad de Cuenca, Cuenca, Ecuador
[3] Programa para el Manejo del Agua y del Suelo (PROMAS), Facultad de Ingeniería Civil, Universidad de Cuenca, Cuenca, Ecuador
[4] Department of Earth and Environmental Sciences, KU Leuven, Leuven, Belgium

ORCID badget of authors and e-mail
Veerle Vanacker: http://orcid.org/0000-0002-8237-3446. E-mail: veerle.vanacker@uclouvain.be
Marie Guns: https://orcid.org/0000-0002-2680-5531. E-mail: marie guns@yahoo.fr
Francois Clapuyt: http://orcid.org/0000-0001-9940-9356. E-mail: francois.clapuyt@uclouvain.be
Vincent Balthazar: https://orcid.org/0000-0002-6515-5359. E-mail: vicent.balthazar@gmail.com
Gustavo Tenorio: http://orcid.org/0000-0001-5306-2166. E.mail: gus.tenoriopoma@kuleuven.be
Armando Molina: http://orcid.org/0000-0002-2599-1061. E-mail: armando.molinav@ucuenca.edu.ec
*Corresponding author

Recibido: 01-07-2019. **Aceptado:** 18-12-2019. **Fecha de publicación on-line:** 02/09/2020

Citation / Cómo citar este artículo: Vanacker, V., Guns, M., Clapuyt, F., Balthazar, V., Tenorio, G., Molina, A. (2020). Spatio-temporal patterns of landslides and erosion in tropical andean catchments. *Pirineos, 175,* e051. https://doi.org/10.3989/pirineos.2020.175001

ABSTRACT: Tropical mountain regions are prone to high erosion rates, due to the occurrence of heavy rainfall events and intensely weathered steep terrain. Landslides are a recurrent phenomenon, and often considered as the dominant erosion process on the hillslopes and the main source of sediment. Quantifying the contribution of landslide-derived sediment to the overall sediment load remains a challenge. In this study, we derived catchment-average erosion rates from sediment gauging data and cosmogenic radionuclides (CRN), and examined their reliability and validity for constraining sediment yields in tectonically active regions. Then, we analysed the relationship between catchment-average erosion rates and landslide-derived sediment fluxes.

The Pangor catchment, located in the western Andean mountain front, was selected for this study given its exceptionally long time series of hydrometeorological data (1974-2009). When including magnitude-frequency analyses of the sediment yields at the measurement site, the corrected gauging-based sediment yields remain one order of magnitude lower than the CRN-derived erosion rates. The underestimation of catchment-average erosion rates from gauging data points to the difficulty of extrapolating flow frequency and sediment rating data in non-stationary hydrological re-

gimes, and severe undersampling of extreme events. In such conditions, erosion rates derived from cosmogenic radionuclides are a reliable alternative method for the quantification of catchment-average sediment yield. Landslide inventories from remote sensing data (1963-2010) and field measurements of landslide geometries are the input data for the derivation of landslide-derived sediment fluxes. The landslide-related erosion rates of 1688^{+901}_{-326} and 630^{+300}_{-108} t.km^2.y^{-1} are similar to the CRN-derived erosion rates, likely indicating that landslides are the main source of sediment in this mountainous catchment.

KEY WORDS: Tropical Andes; extreme event; El Niño Southern Oscillation; Land use change; Sediment transport; Soil erosion; Cosmogenic nuclides; Gauging stations.

RESUMEN: Las cadenas montañosas en las regiones tropicales se caracterizan por las altas tasas de erosión debido a los eventos de lluvia intensa, terrenos escarpados y al alto grado de meteorización del material parental. Los deslizamientos son fenómenos recurrentes, y son considerados como los procesos más importantes de erosión en las zonas montañosas y las principales fuentes de sedimentos en el sistema fluvial. Con el objetivo de cuantificar la contribución de sedimentos provenientes de los deslizamientos al sistema fluvial, se realizó un estudio de caso en la Cuenca del Río Pangór, Ecuador. En este estudio, se cuantificó las tasas de erosión a escala de cuenca por medio de información derivada de estaciones de aforo de caudales e inventarios de isótopos cosmogénicos en sedimentos fluviales. Después, se evaluó la fiabilidad y validez de la información obtenida con el objetivo de cuantificar la carga de sedimento transportado por el río en regiones montañosas. Finalmente, se analizó la fracción de la carga total de sedimento proveniente de deslizamientos en las laderas.

La cuenca del Río Pangór fue seleccionada por su extensa serie de tiempo de datos hidrometeorológicos (1974-2009). La carga de sedimento en el Río Pangór fue estimada por medio de un análisis de magnitud-frecuencia de la información recolectada en una estación hidrométrica y datos de concentración de sedimentos en suspensión. Los resultados muestran un valor de un orden de magnitud menor que la tasa de erosión calculada en función de los inventarios de isótopos cosmogénicos. Esta diferencia se explica por (i) la dificultad de extrapolar la información sobre la frecuencia temporal de los caudales y la carga de sedimento en regímenes hidrológicos no estacionarios, y (ii) el submuestreo de eventos extremos. Bajo estas condiciones, la cuantificación de las tasas de erosión derivadas de los isótopos cosmogénicos proporcionan una metodología alternativa para la cuantificación de la carga total de sedimentos en el sistema fluvial. Un inventario multitemporal (1963-2010) de deslizamientos fue desarrollado a partir de imágenes de satélite y fotografías aéreas. Mediante trabajo de campo se generó información sobre la geometría de los deslizamientos para la cuantificación de volúmenes de sedimento producido por los deslizamientos. En la cuenca del Río Pangór las altas tasas de erosión producida por los deslizamientos varían entre 1688^{+901}_{-326} y 630^{+300}_{-108} t.km^2.y^{-1}, valores que son similares a las tasas de erosión derivadas de isotopos cosmogénicos. Los resultados indican que los deslizamientos son las principales fuentes de sedimento en esta cuenca montañosa.

PALABRAS CLAVE: Andes tropicales; Eventos extremos; El Niño Southern Oscillation; Cambio del uso de la tierra; Transporte de sedimentos; Erosión de suelo; Nucleidos cosmogénicos; Estaciones de aforo.

1. Introduction

Although small mountainous catchments ($< 10 \times 10^3$ km^2) make up a relatively small proportion (estimated at ~10%) of the global terrestrial surface draining to the ocean, they account for about 45% of the global sediment discharge to the oceans (Leithold *et al.*, 2006; Milliman & Farnsworth, 2013). In tectonically active ranges, the combination of high uplift rate, high relief, and rocks fractured by seismic activity can produce very high erosion rates up to 350 mm.kyr^{-1} (Portenga & Bierman, 2011). Landscapes respond to tectonic uplift by fluvial incision and valley deepening, which causes steepening of adjacent hillslopes (Clarke & Burbank, 2010). As hillslope gradients are ultimately limited by their threshold angle of stability, hillslope steepening leads to destabilisation of slopes and the subsequent increase in landslide processes (Korup *et al.*, 2010; Vanacker *et al.*, 2015). In active mountain belts, landslides are known to be a recurrent phenomenon. Amongst them, rainfall-triggered landslides are one of the most widespread natural hazards (Sidle *et al.*, 2006). They are often considered as the dominant erosion process on hillslopes and the principal source of riverine sediment (Schuerch *et al.*, 2006; Molina *et al.*, 2008). However, the contribution of landslides to the overall sedimentary budget is not yet well known and quantitative studies are scarce (Schwab *et al.*, 2008; Bell *et al.*, 2012).

Tropical mountain ranges present unique opportunities to study landslides and sediment transfer mechanisms. Tropical wet mountains are characterised by heavy annual rainfall with rainfall amounts over 3000 mm.yr^{-1} (Chen & Lee, 2003; Siame *et al.*, 2011). During prolonged rainstorm events and high-intensity rainfall, the increased water storage in the soil system triggers landsliding due to an increase in soil weight and pore pressure

and reduction of the shear strength (Montgomery *et al.*, 2002; Vanacker *et al.*, 2003). In addition, the intense physical, chemical and biological weathering in tropical regimes transform the fresh rock into the regolith, thus decreasing the intrinsic rock strength (Borrelli *et al.*, 2007; Che *et al.*, 2012). The combination of steep slopes, deep regolith weathering, and intense rainfall explain the high landslide hazards associated with tropical mountain ecosystems (Hong *et al.*, 2007).

Very few, if any, tropical mountain ecosystems are preserved from human activities (Grau & Aide, 2008; Gleeson *et al.*, 2016). Anthropogenic activities - agriculture, forestry, road building and urban sprawl, tourism, and hydropower development - directly affect sediment production, transport and export (Sidle *et al.*, 2006; Guns & Vanacker, 2014). Although rural population and traditional mountain agriculture began to decrease in various tropical countries (Lambin & Meyfroidt, 2010), many regions are still submitted to severe deforestation practices (Lambin *et al.*, 2004; Hansen *et al.*, 2010). Anthropogenic land cover change has increased the overall landslide hazard and risks (Glade, 2003), with a severe increase in the frequency of shallow landslides (Vanacker *et al.*, 2003; Guns & Vanacker, 2013). For the last two decades (1995-2014), Haque *et al.* (2019) reported a significant global rise in the number of deadly landslides.

In the present study, we quantify the rates of sediment production and transport in a small mountainous catchment based on field data of landslide inventories, sediment gauging data and cosmogenic nuclide inventories of river sediments. This field-based study in the Western Cordillera of Ecuador, allows us to address the following two research questions: Which methods are reliable for estimating catchment-average sediment yield in tropical mountain rivers? What is the contribution of landslide-related sediment to the overall sediment budget? The study catchment was selected because of the existence of an exceptionally long time series of hydrometeorological data for the region with large inter- and intra-annual variability in precipitation. The western Cordillera facing the Pacific Ocean is strongly influenced by El Niño (Vicente-Serrano *et al.*, 2017; Tobar & Wyseure, 2018). Thus, extreme rainfall events are frequent and high inter-annual variability in precipitation is common. Moreover, an analysis of sediment budgets at a regional scale is so far nearly absent in the Ecuadorian western Cordillera. With the exception of e.g. Tote *et al.* (2011), most studies on sediment dynamics in the tropical Andes were done in the Eastern Cordillera, probably because this region is the primary source of sediments for the lower Amazon basin (Vanacker *et al.*, 2007a; Townsend-Small *et al.*, 2008; Tenorio *et al.*, 2018).

2. Materials and Methods

2.1. Study area

The study area is located in the western Cordillera and has an altitude between 1438m and 4427m (Figure 1). The 283km^2 Pangor catchment is delimited to the north by Mt. Chimborazo (6310 m), to the west by the Chimbo River and by the cities of Pallatanga to the south and Riobamba to the east. The mean slope value in the catchment is 25°, with 50% of the area being above this value. These result in steep topography with narrow and deeply incised river valleys. The Pangor river valley crosses the Palatanga right-lateral strike-slip fault, partly visible in the field at elevations above 3600m (Figure 1). Fault slip rates are estimated at 2.9 to 4.6mm.yr^{-1} (Winter *et al.*, 1993).

The climate is equatorial mesothermic with a semi-humid to humid regime (Molina *et al.*, 2015), with precipitation increasing with altitude. Intra-annual variations are characterised by a dry season from June to September and a bimodal rainy season from October to May. Temperatures stay relatively constant throughout the year with a mean annual temperature of 8°C to 20°C depending on altitude. Two pluviometric and one hydrological station from the Instituto Nacional de Meteorología e Hidrología (2009) have exceptionally long time series of precipitation and discharge data for this region. The mean annual precipitation at the Juan de Velasco station (3109 m a.s.l., Figure 1) is about 1400 mm (1970-2009), with high inter-annual variability, from 475mm (2002) to 3700mm (1994). At the Chimbo DJ Pangor station (1452 m a.s.l., Figure 1), the mean annual precipitation was only about 1000 mm.

Soils are developed in volcanic and meta-sedimentary rocks, and are classified as Andisols, Histosols and Mollisols following the USDA soil taxonomy. They are characterised by high organic matter contents and high fertility when undisturbed (Henry *et al.*, 2013; Molina *et al.*, 2019). The land use pattern is the result of several decades of anthropogenic land use changes: at mid and low altitudes, one can observe a patchwork of small agricultural plots, remnants of subalpine cloud forest, and patches of abandoned land with regeneration of shrubs. Patches of montane cloud forest are preserved on steep slopes with low accessibility. At high altitude, páramo grasslands are the dominant vegetation system, although plantation forests with exotic species are rapidly expanding since the 2000s (Balthazar *et al.*, 2015).

2.2. Landslide-related sediment flux

A multi-temporal landslide inventory (1963, 1977, 1989, 2010) was established for two representative subcatchments, Virgen Yacu (11 km²) and Panza (30 km²), located in the middle and lower part of the Pangor catchment (Figure 1). For 1963, 1977 and 1989, landslides were identified and digitised in ArcGIS on orthorectified aerial photographs at 1:60000 scale following the method described in Guns & Vanacker (2014). For 2010, the landslide inventory was established using World View II satellite images with a resolution of 0.5m. To avoid overestimation of landslide numbers, the digital inventory only includes landslides with fresh morphological appearance and poor to no vegetation cover. Relying on field evidence of rapid recolonisation of the landslide scars by vegetation, we assumed

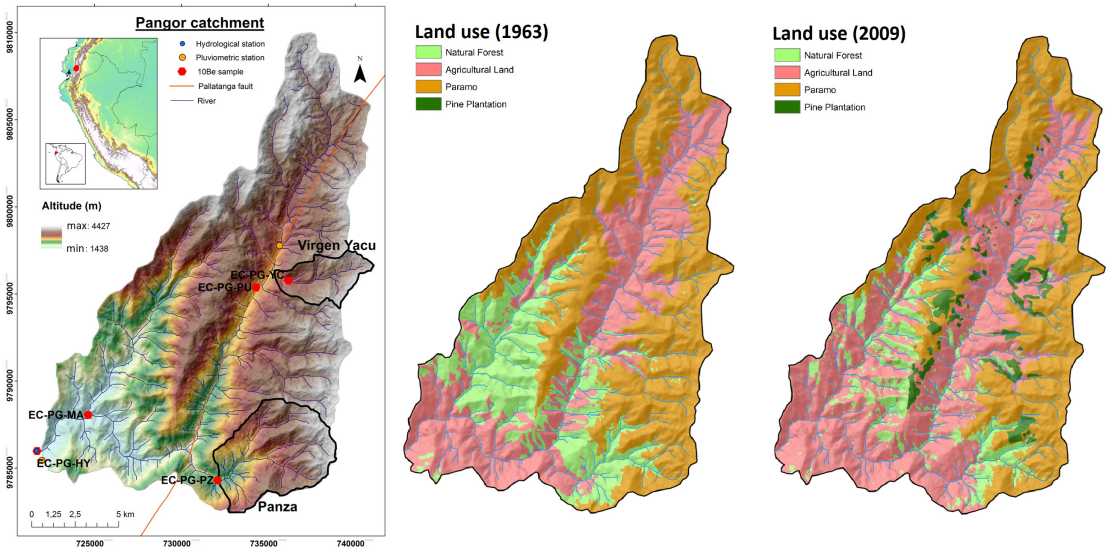

Figure 1: Geomorphic setting of the Pangor catchment in the western Cordillera, with location of the two pluviometric (yellow circle) and one hydrological (blue circle) station. The two sub-catchments, Virgen Yacu and Panza, where the landslide mobilization rates were quantified are delineated in black. The sampling locations for ^{10}Be are shown by red hexagons.

Figura 1: Localización de la cuenca del Rio Pangór en la Cordillera Occidental de los Andes, con la ubicación de las estaciones pluviométricas (amarillo) y la estación hidrométrica. Las dos sub-cuencas, Virgen Yacu y Panza, por las cuales la tasa de producción de sedimentos por deslizamientos fue cuantificada, están delimitadas en el mapa. La localización de los sitios de muestreo para 10Be está demarcada con un hexágono rojo.

that the landslides occurred shortly before the date of image acquisition. The area affected by landslides is here defined as the total disturbed area. Given that it was not always possible to distinguish the erosion and deposition areas on the aerial photographs, the total landslide area might be slightly overestimated.

Landslide volumes were derived from an empirical relationship between the landslide area and volume following (Brunetti *et al.,* 2009). For 32 landslides, the landslide length, width and depth were measured in the field in 2010 and 2011. To represent the landslide form, and also to partly compensate for area overestimation, we decided not to approximate landslides by rectangle parallelepipeds, as many authors e.g. Brunetti *et al.*, (2009) and Guzzetti *et al.* (2009) do, but instead by hemi-ellipsoids. For the 32 landslides for which depth (d), length (l) and width (w) was known, we calculated landslide volume (V) by applying the hemi-ellipsoid formulae (Eq.1):

$$V = \frac{\pi lwd}{6} \quad (1)$$

An empirical relationship can then be obtained between the landslide volume (V) and area (A):

$$V = \alpha \ A^{\gamma} \quad (2)$$

As conversion from log(V) to V creates a systematic bias, half of the residual variance has to be incorporated in the right side of Eq. 2 to correct for volume underprediction. The corrected empirical power-law scaling linking landslide volume (V) to its area (A) is the following:

$$V = \exp\left(\alpha + \gamma \log(A) + \frac{\sigma^2}{2}\right) = \exp\left(\alpha + \frac{\sigma^2}{2}\right) \times A^{\gamma} \quad (3)$$

where α and ϒ are parameter estimates and σ is the residual standard error. This empirical power-law equation (Eq.3) allowed us to estimate the volume of the individual landslides. The total volume of material displaced by the landslides (V_T) is obtained by summing up the values of all individual landslides.

Following Guzzetti *et al.* (2009), the landslide mobilisation rate, φL (mm.yr^{-1}), can be calculated as

$$\varphi_L = \frac{V_T}{t^* A_C} \times 1000 \quad (4)$$

Where V_T is the total volume (m³) of material displaced by landslides over a period of time t (year) and for a given catchment area, A_C (m²). In this study, we use the landslide mobilisation rate as an approximation of the landslide erosion rate, as we do not have information on the proportion of landslide debris that is temporally stored on the slope and the tributary channels. We assume that the landslide material mobilised on the hillslopes is efficiently delivered so that the landslide mass is entirely evacuated within 3 years after the landslide occurrence (Guns & Vanacker, 2013; Clark *et al.*, 2016). This assumption is reasonable: for the 283 landslides in the inventory, the median distance from the landslide runout zone to the river network is less than 75m (Figure 2) pointing to a short and direct connection with the river network.

2.3. Sediment-gauging-based average sediment yield

The average sediment yield at the outlet of the Pangor catchment was derived from the sediment rating curve and flow frequency distribution using techniques described in (Crowder & Knapp, 2005). For the hydrological station Pangor AJ Chimbo (INAMHI, Figure 1), data on daily water discharge ($m^3.s^{-1}$) is available for the period between 1/01/1974 and 31/12/2009 (except for the year 1997). Notwithstanding the exceptionally rich hydrological dataset, sediment data from INAMHI is scarce with only 16 data points on suspended sediment concentration (SSC) during this time period. To overcome this limitation, an intensive data collection was organised in 2011-2012, covering the period between 20/07/2011 and 2/08/2012. During one hydrological year, a local farmer recorded the river stage at the hydrological station every day, and took a 500 ml water sample once a week during the dry season and twice a week during the rainy season. In total, 93 water samples were collected and analysed for suspended sediment concentrations at the University of Cuenca, Ecuador.

By using regression techniques, we derived the sediment rating curve from the plot of the log(suspended sediment concentration) against log(daily water discharge). As conversion from log(SSC) to SSC creates a systematic bias that leads to sediment load underestimation (Ferguson, 1986), half of the residual variance was added to the estimator to correct for underprediction. The corrected sediment rating curve is calculated following Eq. 5

$$SSC = \exp\left(a + b\log(Q) + \frac{\sigma^2}{2}\right) = \exp\left(a + \frac{\sigma^2}{2}\right) \times Q^b \quad (5)$$

where SSC is the suspended sediment concentration ($kg.m^{-3}$), Q is the water discharge ($m^3.s^{-1}$) and a and b are coefficients determined by least squares regression.

The daily discharge data, recorded between 1974 and 2009, are the input data for the flow frequency distribution. The discharge values were classified into equal-size intervals of $\log_{10}(Q)$. The frequency of observed discharges in each class interval was counted and converted in days per year. The results were then plotted as flow frequency (in $d.yr^{-1}$) on the Y-axis against $\log_{10}(Q)$ class intervals on the X-axis. Taking the discharge values as the class midpoints, a mathematical adjustment was performed to find the best flow frequency distribution. The return periods for particular discharges were computed from the flow frequency distribution.

For each discharge class defined above, we estimated the suspended sediment load corresponding to the mid-class discharge value using Eq. 5 and multiplied it by the percentage of time that discharge values of that particular class are predicted to occur per year according to the flow frequency distribution. The total suspended load is then obtained by summing the data over the flow duration curve intervals. By dividing the suspended load by the catchment's area, the average annual suspended sediment yield is derived. In this paper, the suspended sediment yield is expressed in $t.km^{-2}.yr^{-1}$. The advantage of this approach is that it allows us to include discharge values with long recurrence intervals that span beyond the period of observations.

2.4. Cosmogenic 10Be-based erosion rates

Steady state catchment-average denudation rates were derived from the blank-corrected ^{10}Be concentrations in river sediments. In-situ produced cosmogenic ^{10}Be denudation rates integrate over time scales of 10^3 to 10^4 years, and dampen short-term anthropogenic or climatic fluctuations in denudation rates (Vanacker *et al.*, 2007b; Vanacker *et al.*, 2015). The in-situ ^{10}Be concentration at the terrestrial surface is inversely proportional to the denudation rate, and can be assessed from:

$$C = \frac{P_0}{\left(\lambda + \frac{\epsilon\rho}{\Lambda}\right)}$$

Where P_0 is the production rate of ^{10}Be in quartz (atoms g^{-1} yr^{-1}), λ the nuclide decay constant (yr^{-1}), ε the denudation rate (cm yr^{-1}), ρ the density of the material (g cm^{-3}) and Λ the cosmic ray attenuation length (g cm^{-2}). The production rate, P_0, is the result of nuclide production by nucleons, stopped and fast muons (Lal, 1991). The denudation rate, ε, is the combined effect of physical erosion and chemical weathering. In the remaining part of the paper, we refer to the in-situ produced ^{10}Be denudation rates as cosmogenic ^{10}Be-based erosion rates.

Fluvial sediments for ^{10}Be analyses were collected in the active part of the stream channel from the Pangor trunk stream and its main tributaries (Figure 1). Samples were dried and sieved, and pure quartz was extracted from the 500-3000 µm grain size fraction of the alluvial sediment. We refer to (von Blanckenburg *et al.*, 1996) for the separation methods to extract ^{10}Be from pure quartz. Approximately 300 µg of 9Be carrier was added to the ≈20 to 40 g pure quartz. Ratios of $^{10}Be/^{9}Be$ were measured in BeO targets with the accelerator mass spectrometry at ETH Zürich (Kubik & Christl, 2010). The ratios were normalised to the ETH in-house secondary standard S2007N with a nominal value of $^{10}Be/^{9}Be$ of 28.1×10^{-12} (Kubik & Christl, 2010) which is in agreement with a half-life of 1.387 Myr (Chmeleff *et al.*, 2010). From each sample, a laboratory blank with a $^{10}Be/^{9}Be$ ratio of $4.65 \pm 0.50\times10^{-15}$ (n=9) was subtracted. The analytical uncertainties on the $^{10}Be/^{9}Be$ ratios of sample and blank were then propagated into the 1 SD (standard deviation) analytical uncertainty for nuclide concentrations.

In this study, the relative spallogenic and muogenic production rates are based on the empirical muogenic-to-spallogenic production ratios established by Braucher *et al.* (2011), using a fast muon relative production rate at SLHL of 0.87% and slow muon relative production

rate at SLHL of 0.27%. Corrections for skyline shielding were made following Norton & Vanacker (2009). Production rates were scaled following Lal (1991), with a sea level high-latitude production rate of 4.37±0.18 atoms.g^{-1}.yr^{-1} (Martin *et al.*, 2017). The latter represents the regionally averaged SLHL production rate for the Tropical Andes. As the sampled basins were not covered by snow or ice during the denudation integration time scales, no correction was made for snow shielding. The CosmoCalc add-in for Excel (Vermeesch, 2007) was used to calculate the scaling factors and catchment-average denudation rates. The total denudation is the result of physical erosion and chemical weathering. In the remaining part of the text, we refer to the denudation rates derived from in-situ ^{10}Be nuclide as cosmogenic ^{10}Be-based erosion rates.

3. Results

3.1. Landslide-related sediment flux

The multi-temporal landslide inventory contains 283 landslides: 123 in the Virgen Yacu and 160 in the Panza catchment (Table 1). About 0.42% of the total surface area of 41 km² is affected by landslides. Most of the observed landslides can be classified as earth slides (translational slides), earth slumps (rotational slides) or rock falls according to the Cruden & Varnes (1996) classification scheme. Figure 2 shows that the landslide size, characterised by the surface area, is statistically similar in the two catchments (Mann Whitney test, p-value: 0.19). The largest slide is observed in the VirgenYacu catchment, with a surface area of 8522m².

Based on the field measurements on 32 accessible slides, the following empirical landslide volume-area relationship was established (Figure 3):

$$V = 0.237\ A^{1.42} \quad (6)$$

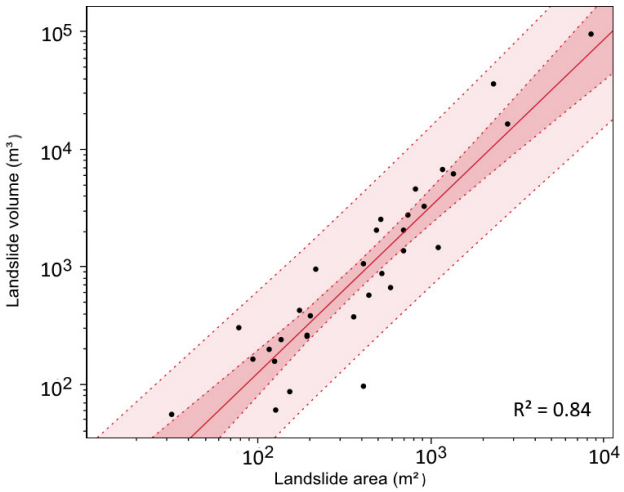

Figure 3: Empirical landslide volume-area relationship, established for the Ecuadorian Andes based on field measurements of 32 representative landslides. The 95% confidence and prediction intervals are plotted on the graph.

Figura 3: Relación empírica entre el área de deslizamientos (A) y el volumen (V) para los Andes ecuatorianos, basados en mediciones en campo de 32 deslizamientos representativos. Los intervalos de confianza y de predicción del 95% están dibujados en el gráfico.

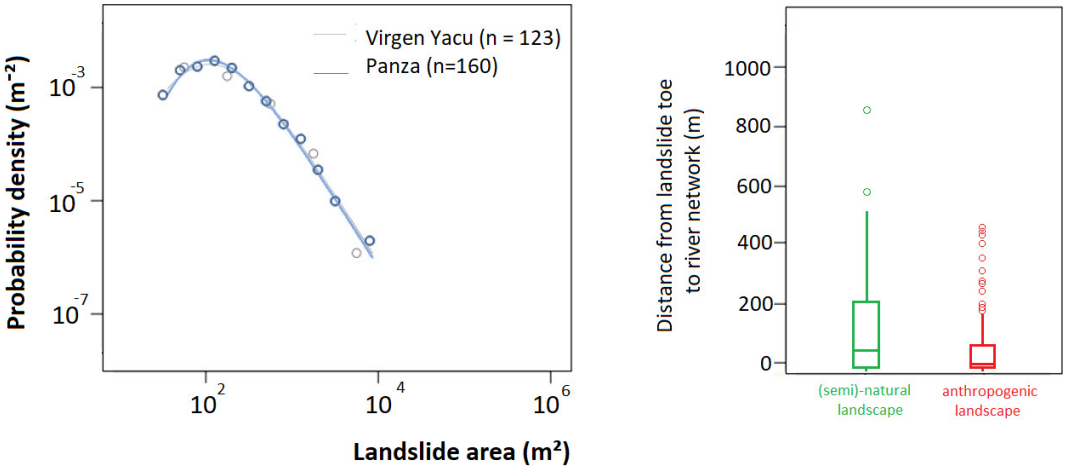

Figure 2: Landslide inventory containing 283 landslides. On the left: Landslide frequency-area distribution of the landslides observed over the period (1963-2010), in the Virgen Yacu and Panza sub-catchments. On the right: Distance between run-out zone and the river network for all landslides located in (semi-)natural and anthropogenic environments.

Figura 2: Inventario de 283 deslizamientos. A la izquierda: la relación entre la frecuencia y el área de afectación de los eventos registrados durante la época 1963-2010, en las sub-cuencas de Virgen Yacu y Panza. A la derecha: distancia entre la base del deslizamiento cubierta por el material acumulado y el cauce del río para los deslizamientos localizados en áreas (semi-)naturales y antropogénicas.

Table 1: Landslide characteristics for the two sub-catchments in the Pangor catchment, based on a multi-temporal landslide inventory (1963, 1977, 1989, 2010).
Tabla 1: Características de deslizamientos observadas en dos sub-cuencas en la cuenca del Río Pangór. Los inventarios multitemporales fueron reconstruidos a partir de imagines de satélite y fotografías aéreas.

	Panza				VirgenYacu			
	1963	**1977**	**1989**	**2010**	**1963**	**1977**	**1989**	**2010**
Number of landslides	13	33	30	84	16	27	11	69
Landslide frequency (count/km^2)	0.44	1.11	1.01	2.92	1.50	2.71	2.06	8.04
Total area affected by landslides (m^2)	8059	13109	11412	44239	9914	27344	15625	39383
Specific area affected by landslides (m^2/km^2)	270	439	382	1483	927	2556	1460	3681
Mean landslide area (m^2)	620	397	380	508	620	943	710	458
Maximum landslide area (m^2)	3246	2776	2269	6423	1399	6008	4582	8522

Where V is the volume of material (m²) displaced by the landslide, and A is the surface area of the landslide (m²). Although the landslide volume-area relationship is based on a limited number of field measurements, the parameter estimates for α and ϒ are in good agreement with the values that were reported by (Guzzetti *et al.*, 2009; Larsen *et al.*, 2010). A comparison of the landslide scaling relationship that we established for the Ecuadorian Andes with those proposed earlier in the literature is shown in Table 2.

The total landslide volume, obtained by integrating the individual landslide volumes estimated using Eq.6 over all landslides observed, equals 3.25 x 10^5 m³ for the Virgen Yacu and 3.39 x10^5 m³ for the Panza catchment (Table 2). These estimates are within 1 SD error of the landslide volume estimates using the empirical landslide scaling relationship established by Larsen *et al.* (2010) for the Himalaya.

When considering the overall time span of observations (1963-2010), the landslide mobilisation rates (derived using Eq. 4) equal 0.63 mm.yr^{-1} for the Virgen Yacu and 0.24 mm.yr^{-1} for Panza catchment. These rates are underestimating the real landslide mobilisation rates because the time series of remote sensing data is erratic: over the 48-year period, landslides were only detected at 4 moments of time (1963, 1977, 1989, and 2010) and correspond to morphologically fresh features. Field observations during the period 2008-2011 revealed that landslide scars are recolonised by vegetation within 2 to 3 years, making them indiscernible on optical remote sensing data after 3 to 4 years. As such, the inventory based on four discrete moments of time is representative for a 12-year time interval, instead of the full 48 years spanning the observation period. To correct for this sampling bias, we multiplied the landslide mobilisation rates by four assuming that landslide processes are homo-

Table 2: The regional landslide scaling relationship established for the Ecuadorian Andes, in comparison with landslide scaling relationships from literature ([1]Larsen *et al.,* 2010; [2] Guzzetti *et al.,* 2009). The table mentions for each landslide scaling relationship the parameters values of Eq. 3 ($V = \alpha A^{\gamma}$), its goodness of fit (R^2), and the sample size (n). The two last columns mention the landslide volume estimates using the respective landslide scaling relationships. The uncertainty on the volume estimate is calculated by propagating a 1 SD error on the ϒ parameter estimate.
Tabla 2: Relación empírica entre el área de deslizamientos (A) y el volumen (V) para los Andes ecuatorianos, y comparación con información de la literatura ([1]Larsen et al., 2010; [2] Guzzetti et al., 2009). La tabla menciona los valores de los parámetros de la ley de potencia (Eq. 3, $V = \alpha A^{\gamma}$), su bondad de ajuste (R^2), y el número de observaciones (n). Las dos últimas columnas indican las estimaciones del volumen total del material que los deslizamientos pueden aportar al cauce. La incertidumbre está calculada por propagación de la desviación estándar de los valores empíricos del parámetro ϒ.

Dataset	**α**	**ϒ ± 1 SD**	**R^2**	**n**	**Total volume (m^3) VirgenYacu (n=123)**	**Total volume (m^3) Panza (n=160)**
Global dataset[1]						
All landslides	0.15	1.33 ± 0.01	0.95	4231	$1.04^{+0.013}_{-0.012} \times 10^5$	$1.10^{+0.010}_{-0.009} \times 10^5$
Soil landslides	0.36	1.15 ± 0.01	0.90	2136	$0.67^{+0.010}_{-0.009} \times 10^5$	$0.73^{+0.008}_{-0.008} \times 10^5$
Bedrock landslides	0.19	1.35 ± 0.01	0.96	604	$1.51^{+0.038}_{-0.035} \times 10^5$	$1.60^{+0.030}_{-0.027} \times 10^5$
Himalaya subset[1]	0.26	1.36 ± 0.01	0.98	428	$2.25^{+0.058}_{-0.053} \times 10^5$	$2.37^{+0.044}_{-0.044} \times 10^5$
Global dataset[2]	0.07	1.45 ± 0.01	0.97	677	$1.01^{+0.544}_{-0.196} \times 10^5$	$1.06^{+0.393}_{-0.149} \times 10^5$
This study	0.24	1.42 ± 0.12	0.84	32	$3.25^{+1.740}_{-0.627} \times 10^5$	$3.39^{+1.260}_{-0.478} \times 10^5$

geneous through time. Table 3 shows the corrected landslide mobilisation rates with their uncertainties. The corrected values equal $2.53^{+1.35}_{-0.49}$ and $0.95^{+0.35}_{-0.13}$ mm.yr^{-1} for the Virgen Yacu and Panza catchments respectively, and are of the same magnitude than those reported by Muenchow *et al.* (2012) for the southern Ecuadorian Andes. To facilitate comparison with sediment yields derived from sediment gauging and in-situ ^{10}Be cosmogenic nuclides, the landslide mobilisation rate was converted to t.km^{-2}.yr^{-1}. Here, a bulk density of 2 g.cm^{-3} is used assuming that the mobilised material is a mixture of soil (with a mean density of 1.3 g.cm^{-3}) and weathered bedrock (with density of 2.7 g.cm^{-3}). After correcting for landslide runout, landslide-related sediment fluxes equal 1688^{+901}_{-326} and 630^{+300}_{-108} t.km^{-2}.yr^{-1} for the Virgen Yacu and Panza catchments respectively.

3.2. Sediment-gauging-based average sediment yield

The sediment rating curve is based on 109 measurements of suspended sediment concentration at the Pangor AJ Chimbo gauging station: 16 data points collected by INAMHI over the period 1979-2002, and 93 data points by our team over the period July 2011 and August 2012 (Figure 4). Figure 5 shows the best fit (R^2=0.30) obtained for the log-log plot of suspended sediment concentration, SSC (kg.m^{-3}) against water discharge, Q (m^3.s^{-1}):

$$SSC = 4.76 \times 10^{-3}\ Q^{1.63} \quad (7)$$

The relatively low R^2 statistic points to significant scatter in the data, which is not atypical for small to medium-sized mountain rivers (Latrubesse & Restrepo, 2014; Vanacker *et al.*, 2007a; Rosas *et al.*, 2020). This is probably a reflection of the flashy regime of the Pangor River, causing large variability in discharge and suspended sediment concentration through time.

The 12784 daily discharge data observed during the time period 1974-2009 were used to calculate the flow frequency distribution (in d.yr^{-1}). Using a class size of 0.2 $\log_{10}$(Q), twenty-one classes cover the range of observed $\log_{10}$(Q) (Figure 6). The best statistical adjustment corresponds to the combination of two normal distributions having approximately the same mean but strongly different dispersion. The empirical relationship provides a good representation of the reality:

$$d = 63{,}12\ e^{-\frac{(log_{10}(Q)-0{,}63)^2}{0{,}04}} + 43{,}04\ e^{-\frac{(log_{10}(Q)-0{,}64)^2}{0{,}36}} \quad (8)$$

where d (d.yr^{-1}) is the number of days per year when a discharge Q (m^3.s^{-1}) occurred.

To account for rare but extreme discharge values in the derivation of the average sediment yield, we extended the

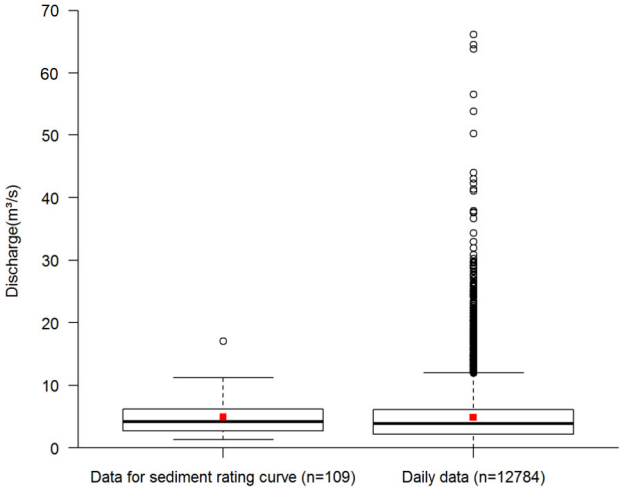

Figure 4: Summary of the daily discharge data collected in the period (1974-2009) and the discharges at which 109 sediment samples were collected. The red dots correspond to the average values.
Figura 4: Resumen de los datos de caudales diarios recolectados en el periodo 1974-2009, y los caudales durante las cuales se recolectó 109 muestras de agua. Los puntos rojos se refieren a los valores promedios.

Table 3: Landslide mobilization rate estimated from landslides inventory of 1963-2010. The uncertainty on the volume estimates is calculated by propagating a 1 SD error on the ϒ parameter estimate using Eq. 6. Landslide-related sediment fluxes are derived from the landslide mobilisation rates, assuming that the landslide mass is entirely evacuated within 3 years after landslide occurrence.
Tabla 3: Producción de sedimentos por deslizamientos con base en el inventario multitemporal de 1963-2010. La incertidumbre en las estimaciones está calculada por propagación de la desviación estándar de los valores empíricos del parámetro ϒ utilizando la ecuación 6. La tasa de erosión causada por deslizamientos ha sido derivada de la tasa de producción de sedimentos por deslizamientos, asumiendo que el volumen de material acumulado se ha evacuado en los primeros 3 años después del evento.

	Landslide mobilization rate ± 1 SD		**Landslide-related erosion**
	(mm/year)	**(t/km^2.year)**	**(t/km^2.year)**
VirgenYacu	$2.53^{+1.35}_{-0.49}$	5063^{+2704}_{-977}	1688^{+901}_{-326}
Panza	$0.95^{+0.35}_{-0.13}$	1891^{+702}_{-267}	630^{+300}_{-108}

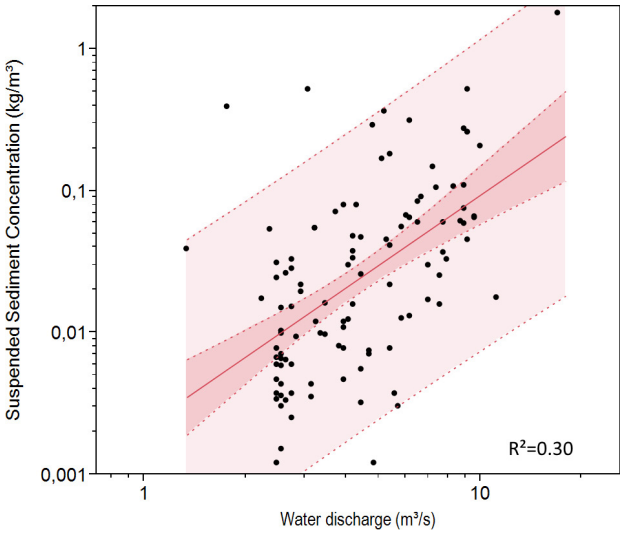

Figure 5: Empirical relationship linking the suspended sediment concentration and water discharge (n=109). The 95% confidence and prediction intervals are plotted on the graph.

Figura 5: Relación empírica entre el caudal y la concentración de sedimentos en suspensión en las muestras de agua del río (n=109). Los intervalos de confianza y de predicción del 95% están dibujados en el gráfico.

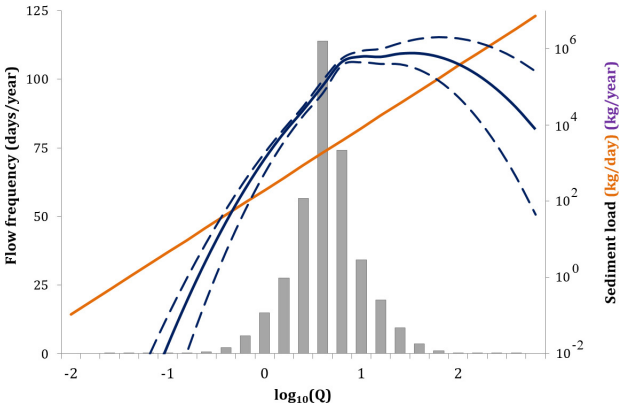

Figure 6: Gauging-based sediment load (kg/year, blue line) in function of $\log_{10}$(discharge). The mean sediment load per discharge class is obtained from the multiplication of the sediment rating curve (orange) and the flow frequency (grey bars). The dots represent the values for the midpoints of each discharge interval, and the curves are the distributions adjusted to the data.

Figura 6: Carga de sedimentos en la estación de aforo (kg/año, linea azul) en función de $\log_{10}$(caudal). La carga promedio de sedimentos por categoría de caudal ha sido obtenida de la multiplicación de la curva de descarga de sedimento (color naranja) y la curva de frecuencia de caudales (barres gris). Los puntos representan los valores para los puntos medios de cada intervalo de caudales, y las curvas son ajustadas a los datos.

range of recurrence intervals to 1000 years (d = 0.001). Using Eq. 8, the discharge with a 1000-year recurrence interval was estimated at 398 $m^3.s^{-1}$. At the river section of the Pangor AJ Chimbo gauging station, the 1000-year flood corresponds to a water height of 3.73 m. The high flood marks that we observed along the river channel in 2012 indicate that this flood peak discharge is entirely reasonable.

Figure 6 shows the yearly sediment loads per discharge class, and the associated 1 SD errors on the estimates. The values are obtained from multiplying the daily-suspended sediment loads estimated with Eq.7 with the flow frequency estimated with Eq.8. The statistical fit shows a humped curve, with a sediment load peak around Q = 25 $m^3.s^{-1}$ (Figure 6), corresponding to the effective discharge. The average transported load decreases at higher discharge, because of rapidly decreasing flow frequency. The integration of the yearly sediment loads over the discharge classes gives the sediment-gauging average sediment yield that

Table 4: ^{10}Be Cosmogenic nuclide-derived erosion rates for 5 drainage basins in the Pangor catchment[a]

Tabla 4: Tasas de erosión derivadas de isotopos cosmogénicos de ^{10}Be de cinco cuencas hidrográficas dentro de la cuenca del Rio Pangor[a].

Nr	ID	Sample	Area km²	Lat, DD	Long, DD	^{10}Be production, at/g_{qtz}/a	^{10}Be/^{9}Be ratio	1σ %	^{10}Be conc at/g_{qtz}	1σ ^{10}Be conc at/g_{qtz}	^{10}Be erosion rate, mm/kyear			^{10}Be sediment yield, t/km²/year
1	ZB8912	PG-YC[1]	11	-1.846	-78.877	28.6	$1{,}42\times10^{-14}$	13	2.37×10^{4}	4.81×10^{3}	758	±	154	1516 ± 308
2	ZB8911	PG-PZ[1]	30	-1.950	-78.913	24.1	$3{,}92\times10^{-14}$	7.8	3.80×10^{4}	3.48×10^{3}	400	±	37	800 ± 74
3	ZB9340	PG-MA	209	-1.843	-78.907	20.5	$5{,}70\times10^{-15}$	44	< LOD					
4	ZB9341	PG-PU	91	-1.796	-78.874	28.3	$1{,}19\times10^{-14}$	17	1.27×10^{4}	3.61×10^{3}	1404	±	401	2808 ± 802
5	ZB8910	PG-HY[1]	281	-1.935	-79.008	21.9	$5{,}00\times10^{-15}$	23	< LOD					
	ZB9339	PG-HY[2]					$6{,}60\times10^{-15}$	34	2.57×10^{3}	2.88×10^{3}	5357	±	5997	10714 ± 11996

[a] Sediment samples were collected from riverbed deposits. For one location (outlet, Pangor AJ Chimbo station), we analysed the effect of the grain size fraction of the ^{10}Be concentration of the alluvial material ([1]0.5–2.0 mm, [2]2.0–3.0 mm). No significant difference in ^{10}Be concentration was observed between grain size fractions. The remaining ^{10}Be analyses were realized on the 0.5–2.0 or 2.0-3.0 mm fraction, depending on the availability of sample material. Typical sample weights were c. 10-15 g and c. 300 µg of ^{9}Be carrier was added to each sample. Given the measured ^{10}Be/^{9}Be ratio in the blanks of $4.65 \pm 0.50\times10^{-15}$, the concentrations and erosion rates are not reported for samples having ^{10}Be concentrations below the detection limit (LOD = 6.13×10^{-15}).

equals $16.3^{+39.0}_{-7.7}$ t.km^{-2}.yr^{-1}, with the uncertainties calculated based on the standard errors on the scaling exponents in Eq.7 and 8.

3.3. Cosmogenic ^{10}Be-based erosion rates

The measured ^{10}Be/^{9}Be ratio, the ^{10}Be concentrations, the corresponding analytical errors and uncertainties are listed in Table 4. The ^{10}Be/^{9}Be ratios of the six alluvial samples are all below 1×10^{-134}. There is no measurable grain size effect on the ^{10}Be concentrations, based on the measurements of ^{10}Be in the sand (0.5 – 2.0 mm) and fine gravel (2.0 – 3.0 mm) fractions. For two of the six samples (PG-HY^{1}, PG-MA), the ^{10}Be concentrations are below the detection limit (LOD). The long-term catchment-average erosion rates range between 400 and 5357 mm.kyr^{-1}, and integrate over 160 to 2000 years. For the samples with ^{10}Be/^{9}Be ratios below 1×10^{-14}, the background of $4.65 \pm 0.50\times10^{-15}$ limits the accuracy of the ^{10}Be analyses and derived erosion rates. The lowest rates correspond to the tributary catchments of Panza (400 ± 37 mm.kyr^{-1}) and Virgen Yacu (758 ± 154 mm.kyr^{-1}), on the east of the trunk stream. The erosion rates for the trunk stream are systematically higher, with rates of 1404 ± 401 mm.kyr^{-1} at the middle segment of the trunk stream and 5357 ± 5997 mm.kyr^{-1} at the outlet of the Pangor basin.

4. Discussion

4.1. Proxies for sediment yield at catchment scale

Sediment yields based on sediment gauging are first-order proxies for the suspended sediment yield. By incorporating information on the flow frequency distribution, it is theoretically possible to estimate the average sediment yield at annual and centennial time scale. However, the derivation of centennial erosion rates strongly hinges on (i) the assumption of stationarity in the flood records, and (ii) the reliability of the sediment rating curve for extreme floods. First, it is likely that decadal climate variability due to the influence of ENSO in the Pangor basin will affect the assumption of stationary in our flood frequency analysis (Machado *et al.*, 2015; Molina *et al.*, 2015). Second, the sediment rating curve is based on 109 measurements of total suspended solids. Although the flow rates at the 109 sampling dates are not significantly different (at 95% confidence interval) from the daily flow rates observed between 1974 and 2009, it is clear from Figure 4 that they underrepresent the high and very high flow rates. The maximum discharge observed during the time period 1974 to 2009 is 66.1 m^3.s^{-1} (during the 1998 El Niño), while the water sample at highest flow rate was taken at a discharge of 17 m^3.s^{-1} only (March 1983). Also, sediment sampling was very limited during the most influential recorded El Niño-Southern Oscillation Event of 1997-98 (Tobar & Wyseure, 2018), when the annual precipitations of 1996 and 1997 were three times higher than the mean annual precipitation in Pangor (INAMHI, 2009). We, therefore, pose that the methods based on sediment gauging data strongly underestimate the suspended sediment yield. As such, the sediment-gauging average sediment yield that equals $16.3^{+39.0}_{-7.7}$ t.km^{-2}.yr^{-1} is a minimum estimate of the average suspended sediment yield.

Besides, the suspended sediment represents only a fraction of the river's total sediment load that comprises the dissolved, suspended load and bed load. Two recent studies in Ecuador (Armijos *et al.*, 2013; Tenorio *et al.*, 2018) highlighted the importance of dissolved load. They showed that for one ton of sediment transported in suspension, 0.5 to 2 ton of solutes are transported as dissolved load. As for the dissolved load, information on the material transported as bedload is unavailable for most gauging stations in the Andes (Latrubesse & Restrepo, 2014). Bedload transport in steep Andean rivers along the western margin of the Andes can be very high, as shown by Link *et al.* (2002). Based on the work pursued by Link *et al.* (2002) and Pepin *et al.* (2010) in the BioBio River, Latrubesse and Restrepo (2014) suggested that the bed load sediments might account for about 75% of the total sediment load in Andean rivers. By assuming a ratio of the dissolved-to-suspended yield of 2 (Tenorio *et al.*, 2018) and bedload-to-suspended yield of 3 (Latrubesse & Restrepo, 2014), we obtain a preliminary estimate of the gauging-based total sediment yield of $81.3^{+197.0}_{-38.8}$ t.km^{-2}.yr^{-1}.

Erosion rates based on ^{10}Be cosmogenic nuclides range between 400 ± 37 and 5357 ± 5997 mm.kyr^{-1} or 800 ± 74 and 10714 ± 11996 t.km^{-2}.yr^{-1} (Table 4). These rates are notably higher than the ^{10}Be-based erosion rates that were published for river sediments in the southern Ecuadorian Andes (Vanacker *et al.*, 2007b; 2015), northern Peru (Abbühl *et al.*, 2011) and northern Chile (Starke *et al.*, 2017). However, they are within the range of ^{10}Be-based erosion rates of active mountain ranges. For example Lupker *et al.* (2012) reported rates of 500 to 2400 mm.kyr^{-1} for the Himalaya, and Norton *et al.* (2011) rates of 170 to 1400 mm.kyr^{-1} for the Alps.

The derivation of erosion rates from ^{10}Be concentrations in river sediments is conditional on several assumptions described in Dosseto & Schaller (2016). In the Pangor catchment, the assumptions of minimal sediment storage, uniform quartz-bearing lithology, and absence of quartz enrichment during erosion processes are all validated. Yet, the sediment cosmogenic nuclide budget might be affected by the occurrence of landslides that supply material that is shielded at depth and poor in cosmogenic nuclides to the river. Model simulations (Niemi *et al.,* 2005; Yanites *et al.,* 2009) showed that this landslide bias in the isotopic system can lead to an overestimation of the ^{10}Be-derived erosion rates, particularly when (1) deep landslides (depth > 5m) dominate the landslide signal and (2) catchments drain areas smaller than 50 to 75 km^2. Figure 2 illustrates that the majority of landslides are smaller than 10^3 m^2, and remove material over a depth of less than 0.8 m. As the landscape is domi-

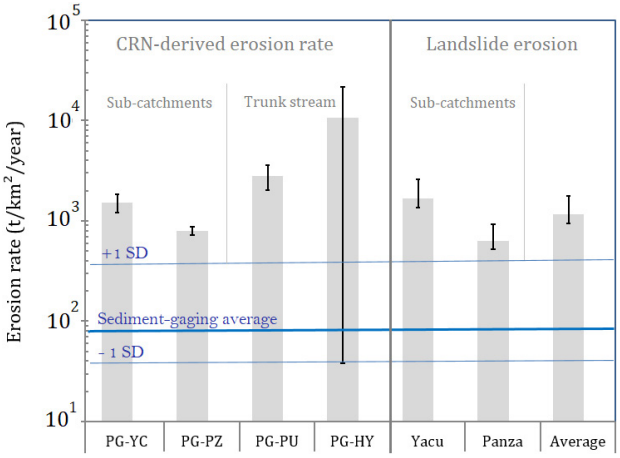

Figure 7: Comparison of landslide-related sediment flux with ^{10}Be-derived erosion rates for four locations (PG-YC, PG-PZ, PG-PU and PG-HY). The sediment-gauging average sediment yield (± 1 SD) is shown by the blue line.

Figura 7: Comparación entre las tasas de erosión causada por deslizamientos y las tazas de erosión derivadas de isotopos cosmogénicos de 10Be de cuatro puntos de muestreo (PG-YC, PG-PZ, PG-PU and PG-HY). La carga promedio de sedimentos de la estación de aforo (± 1 desviación estándar) está indicada por una línea azul.

nated by shallow landslides, the estimated ^{10}Be-derived erosion rates are reliable proxies of the long-term catchment-average erosion.

When comparing the stream gauge-derived and ^{10}Be-derived erosion rates, we observe significant discrepancies between them (Figure 7). The ^{10}Be-derived erosion rates are 5 to > 50 times larger than the gauging-based total erosion rates (Table 4). As they integrate over 160 to 2000 years, they include the impact of extreme phases of the El Niño-Southern Oscillation that were reported to have occurred in 1790-91, 1877-78 (Arteaga *et al.*, 2006), 1924-25 and 1997-98 (Tobar & Wyseure, 2018). During extreme ENSO events, the annual suspended sediment yield can increase by 3 to 60 times, as shown by Morera *et al.* (2017) in the northwestern part of Peru. Contrary to the ^{10}Be-derived erosion rates, the stream-gauge derived sediment yield does not adequately account for sediment transport during high and very high floods. Hence, we consider that the ^{10}Be-derived erosion rates provide more realistic proxies of the geomorphic process rates.

4.2. Contribution of landslide-related erosion to catchment-average erosion rate

From the landslide inventory, the landslide mobilisation rate was estimated at 5063^{+2704}_{-977} and 1891^{+702}_{-267} t.km^{-2}.yr^{-1} for the Virgen Yacu and Panza catchment, respectively. The landslide mobilisation rate is systematically higher than the landslide-related erosion, as only a fraction of the displaced material is removed by fluvial processes and exported from the catchment. In the study sites, the landslide run-out deposits are located at less than 75m from the river network for > 50% of the inventoried slides (Figure 2). Hence, we can reasonably assume that the landslide deposits are evacuated within 2 to 3 years after landslide occurrence, in accordance with previous work on storm-triggered landslides in the Peruvian Andes by Clark *et al.* (2016). After correction, we obtain landslide-related erosion rates of 1688^{+901}_{-326} and 630^{+300}_{-108} t.km^{-2}.yr^{-1} for the Virgen Yacu and Panza catchments respectively (Table 3). The difference in landslide-related sediment flux between the two tributary catchments is a result of the higher landslide density in VirgenYacu compared to Panza catchment (Table 1).

For the two subcatchments with detailed landslide inventories, the landslide-related erosion rates are similar to the CRN-derived erosion rates (Figure 7). It shows that landslides are a major source of sediments in these upland catchments and a main, if not the main, hillslope process in this high-relief tropical environment. This result is in agreement with data from the Luquillo experimental catchment in Puerto Rico, where Larsen (1997) showed that episodic landslides are the dominant source of sediment and they contribute to more than 90% of the total sediment yield at the catchment scale.

The difference between the average landslide-derived sediment flux and the ^{10}Be-derived erosion rates seems to increase with increasing catchment area. Figure 7 shows that the difference becomes particularly large at the outlet of the Pangor catchment, where the ^{10}Be-derived erosion rate is about 9 times greater than the average landslide-derived erosion. Given the active tectonic setting of the area, with the Pangor River draining the western Andes mountain front, the increase in CRN-derived erosion rate downstream is not surprising as was found by Vanacker *et al.* (2015). Downstream of sampling point PG-PU, the Pangor River rapidly steepens in a broad knickzone (Figure 1) where a variety of knickpoints are present in the trunk stream and tributaries. The enhanced fluvial erosion in the knickzone requires the adjacent hillslopes to adjust by frequent landsliding.

5. Conclusion

This case study of the Pangor River catchment illustrates the erosion dynamics along the western Andean mountain front in the tropical Andes. Landslide inventories that were established from remote sensing data for two tributary catchments enabled us to quantify the landslide mobilisation rate that ranged between $0.95^{+0.35}_{-0.13}$ and $2.53^{+1.35}_{-0.49}$ mm per year. The fact that the landslide-related sediment fluxes are similar to the ^{10}Be-derived erosion rates shows that landslides are the principal source of sediment in the upstream catchments. The Pangor River, being a transverse river draining the western mountain front, is characterised by a 10-fold increase in ^{10}Be-derived erosion rates downstream. Landslide magnitude-frequency is also expected to increase in the knickzone, but further studies are needed to verify this hypothesis.

The use of gauging data from hydrological stations is a widely accepted technique to infer sediment discharge from mountain regions to coastal lowlands and oceans. However, our study calls attention to the difficulty of extrapolating flow frequency and sediment rating curves in areas with non-stationary flood frequencies associated with extreme ENSO events. Significant underestimation is reported here for the Pangor River, with sediment gauging-based average sediment yields being roughly one order of magnitude lower than the landslide-related sediment fluxes and the ^{10}Be-derived erosion rates. Given their longer integration time, ^{10}Be-derived erosion rates provide more robust estimates of the catchment-average erosion rates, and allow one to overcome errors associated with systematic under-sampling of extreme flood events in hydrological stations.

Acknowledgements

Data collection and logistic support was provided by the FOMO project funded by the Belgian Science Policy through its Research Program for Earth Observation Stereo II (contract SR/00/133), and the ARES PRD project funded by the Academie de Recherche et Enseignement Supérieur de la Fédération Wallonie-Bruxelles, Belgium at the University of Cuenca, Ecuador. M. Guns was funded through a PhD fellowship from the Fonds National de la Recherche Scientifique (FRS-FNRS, Belgium). She received the Prize for Tropical Geography Yola Verhasselt of the Royal Academy for Overseas Sciences (Belgium) to support her field campaign in Ecuador. The authors would like to thank Mrs Paguay for collecting the water samples during 2011-2012.

References

Abbühl, L.M., Norton, K.P., Jansen, J.D., Schlunegger, F., Aldahan, A. & Possnert, G., 2011. Erosion rates and mechanisms of knickzone retreat inferred from ^{10}Be measured across strong climate gradients on the northern and central Andes Western Escarpment. *Earth Surface Processes and Landf*orm, 36: 1464–1473.

Armijos, E., Laraque, A., Barba, S., Bourrel, L., Ceron, C. Lagane, C., Magat, P., Moquet, S., Pombosa, R., Sondag, F., Vauchel, P., Vera, A. & Guyot, J.L., 2013. Apports de matiéres en suspension et de solides dissous des les bassins andins de l'Equateur. *Hydrological Sciences Journal*, 58(7): 1478–1494. doi: 10.1080/02626667.2013.826359.

Arteaga, K., Tutasi, P. & Jimenez, R., 2006. Climatic variability related to El Nino in Ecuador - a historical background. *Advances in Geosciences*, 6: 237-241.

Balthazar, V., Vanacker, V., Molina, A. & Lambin E.F., 2015. Impacts of forest cover change on ecosystem services in high Andean mountains. *Ecological Indicators*, 48: 63-75. doi: 10.1016/j.ecolind.2014.07.043.

Bell, R., Petschko, H., Röhrs, M. & Dix, A., 2012. Assessment of landslide age, landslide persistence and human impact using airborne laser scanning digital terrain models. *Geografiska Annaler, Series A: Physical Geography*, 94(1): 135–156. doi: 10.1111/j.1468-0459.2012.00454.x.

Borrelli, L., Greco, R. & Gullà, G., 2007. Weathering grade of rock masses as a predisposing factor to slope instabilities: Reconnaissance and control procedures. *Geomorphology*, 87(3): 158–175. doi: 10.1016/j.geomorph.2006.03.031.

Braucher, R., Merchel, S., Borgomano, J. & Bourles, D.L., 2011. Production of cosmogenic radionuclides at great depth : A multi element approach. *Earth and Planetary Science Letters*, 309(1–2): 1–9. doi: 10.1016/j.epsl.2011.06.036.

Brunetti, M.T., Guzzetti, F. & Rossi, M., 2009. Probability distributions of landslide volumes. *Nonlinear Processes in Geophysics*, 16(2): 179–188. doi: 10.5194/npg-16-179-2009.

Che, V.B., Fontijn, K., Ernst, G.G., Kervyn, M., Elburg, M., Van Ranst, E. & Suh, C.E., 2012. Evaluating the degree of weathering in landslide-prone soils in the humid tropics: The case of Limbe, SW Cameroon. *Geoderma,* 170: 378–389. doi: 10.1016/j.geoderma.2011.10.013.

Chen, H. & Lee, C.F., 2003. A dynamic model for rainfall-induced landslides on natural slopes. *Geomorphology*, 51(4): 269–288. doi: 10.1016/S0169-555X(02)00224-6.

Chmeleff, J., von Blanckenburg, F., Kossert, J. & Jakob, D., 2010. Determination of the ^{10}Be half-life by multicollector ICP-MS and liquid scintillation counting. *Nuclear Instruments and Methods in Physics Research, Section B*, 268(2): 192–199. doi: 10.1016/j.nimb.2009.09.012.

Clark, K.E., West, A.J., Hilton, R.G., Asner, G.P., Quesada, C.A., Silman, M.R., Saatchi, S.S., Farfan-Rios, W., Martin, R.E., Horwath, A.B., Halladay, K., New, M. & Malhi, Y., 2016. Storm-triggered landslides in the Peruvian Andes and implications for topography, carbon cycles, and biodiversity. *Earth Surface Dynamics*, 4(1): 47–70. doi: 10.5194/esurf-4-47-2016.

Clarke, B. & Burbank, D.W., 2010. Bedrock fracturing, threshold hillslopes, and limits to the magnitude of bedrock landslides. *Earth and Planetary Science Letters,* 297(3–4): 577–586. doi: 10.1016/j.epsl.2010.07.011.

Crowder, D.W. & Knapp, H.V., 2005. Effective discharge recurrence intervals of Illinois streams. *Geomorphology*, 64(3–4): 167–184. doi: 10.1016/j.geomorph.2004.06.006.

Cruden, D.M. & Varnes, D.J., 1996. *Landslides: investigation and mitigation.* Transportation Research Board Special Report, 247.

Dosseto, A. & Schaller, M., 2016. The erosion response to Quaternary climate change quantified using uranium isotopes and in situ-produced cosmogenic nuclides. *Earth-Science Reviews*, 155: 60–81. doi: 10.1016/j.earscirev.2016.01.015.

Glade, T., 2003. Landslide occurrence as a response to land use change: a review of evidence from New Zealand. *Catena*, 51(3-4): 297–314.

Gleeson, E.H., Wymann von Dach, S., Flint, C.G, Greenwood, G.B, Price, M.F., Balsiger, J., Nolin, A & Vanacker, V, 2016. Mountains of Our Future Earth: Defining Priorities for Mountain Research—A Synthesis From the 2015 Perth III Conference. *Mountain Research and Development*, 36(4): 537–548. doi: 10.1659/MRD-JOURNAL-D-16-00094.1.

Grau, H.R. & Aide, M., 2008. Globalization and Land-Use Transitions in Latin America. *Ecology and Society*, 13(2): 16.

Guns, M. & Vanacker, V., 2013. Forest cover change trajectories and their impact on landslide occurrence in the tropical Andes. *Environmental Earth Sciences*, 70(7): 2941-2952. doi: 10.1007/s12665-013-2352-9.

Guns, M. & Vanacker, V., 2014. Shifts in landslide frequency-area distribution after forest conversion in the tropical Andes. *Anthropocene*, 6: 75-85. doi: 10.1016/j.ancene.2014.08.001.

Guzzetti, F., Ardizzone, F., Cardinali, M., Rossi, M., Valigi, D., 2009. Landslide volumes and landslide mobilization rates in Umbria, central Italy. *Earth and Planetary Science Letters*, 279(3–4): 222–229. doi: 10.1016/j.epsl.2009.01.005.

Hansen, M.C., Stehman, S.V & Potapov, P.V., 2010. Quantification of global gross forest cover loss. *Proceedings of the National Academy of Sciences*, 107(19): 8650–8655. doi: 10.1073/pnas.0912668107.

Haque, U., da Silva, P.F., Devoli, G., Pilz, J., Zhao, B., Khaloua, A., Wilopo, W., Andersen, P., Lu, P., Lee, J., Yamamoto, T., Deellings, D., Wu, J.H., Glas, G.E., 2019. The human cost of global warming: Deadly landslides and their triggers (1995–2014). *Science of the Total Environment*, 682: 673–684. doi: 10.1016/j.scitotenv.2019.03.415.

Henry, A., Mabit, L., Jaramillo, R.E., Cartagena, Y. & Lynch, J.P., 2013. Land use effects on erosion and carbon storage of the Río Chimbo watershed, Ecuador. *Plant and Soil*, 367(1–2): 477–491. doi: 10.1007/s11104-012-1478-y.

Hong, Y., Adler, R. & Huffman, G., 2007. Use of satellite remote sensing data in the mapping of global landslide susceptibility. *Natural Hazards*, 43(2): 245–256. doi: 10.1007/s11069-006-9104-z.

Korup, O., Densmore, A.L. & Schlunegger, F., 2010. The role of landslides in mountain range evolution. *Geomorphology*, 120(1–2): 77–90. doi: 10.1016/j.geomorph.2009.09.017.

Kubik, P.W. & Christl, M., 2010. ^{10}Be and ^{26}Al measurements at the Zurich 6 MV Tandem AMS facility. *Nuclear Instruments and Methods in Physics Research, Section B*, 268(7–8): 880–883. doi: 10.1016/j.nimb.2009.10.054.

Lal, D., 1991. Cosmic ray labeling of erosion surfaces: in situ nuclide production rates and erosion models. *Earth and Planetary Science Letters*, 104(2-4): 424-439.

Lambin, E.F., Geist, H.J. & Lepers, E., 2004. Dynamics of land use and land cover change in Tropical regions. *Annual Review of Environment and Resources*, 28(1): 205–241. doi: 10.1146/annurev.energy.28.050302.105459.

Lambin, E.F. & Meyfroidt, P., 2010. Land use transitions: Socio-ecological feedback versus socio-economic change. *Land Use Policy*, 27(2): 108–118. doi: 10.1016/j.landusepol.2009.09.003.

Larsen, M.C., 1997. *Tropical geomorphology and geomorphic work: A study of geomorphic processes and sediment and water budgets in montane humid-tropical forested and developed watersheds*, *Puerto Rico*. Unpublished Ph.D. thesis, University of Colorado, Geography Department, 341 p.

Larsen, I. J., Montgomery, D.R. & Korup, O., 2010. Landslide erosion controlled by hillslope material. *Nature Geosciences*, 3(4): 247–251. doi: 10.1038/ngeo776.

Latrubesse, E.M. & Restrepo, J.D., 2014. Sediment yield along the Andes: continental budget, regional variations, and comparisons with other basins from orogenic mountain belts. *Geomorphology*, 216: 225–233. doi: 10.1016/j.geomorph.2014.04.007.

Leithold, E.L., Blair, N.E. & Perkey, D.W., 2006. Geomorphologic controls on the age of particulate organic carbon from small mountainous and upland rivers. *Global Biogeochemical Cycles*, 20(3): GB3022. doi: 10.1029/2005GB002677.

Link, O., Cecioni, A., Duyvestein, A. & Vargas, J., 2002. Hydrology of the bio bio river. *Zeitschrift fur Geomorphologie,* 129: 31–39.

Lupker, M., Blard, P.H., Lavé, J., Lanord, C.F., Leanni, L., Puchol, N., Charreau, J. & Bourles, D., 2012. ^{10}Be-derived Himalayan denudation rates and sediments budgets in the Ganga basin. *Earth and Planetary Science Letters*, 333-334: 146-156. doi: 10.1016/J.epsl.2012.04.020.

Machado, M.J., Botero, B.A., Lopez, J., Frances, F., Diez-Herrero, A. & Benito, G., 2015. Flood frequency analysis of historical flood data under stationary and non-stationary modelling. *Hydrology and Earth System Sciences*, 19(6): 2561–2576. doi: 10.5194/hess-19-2561-2015.

Martin, L.C.P., Blard, P.H., Balco, G., Lavé, J., Delunel, R., Lifton, N. & Laurent, V., 2017. The CREp program and the ICE-D production rate calibration database: A fully parameterizable and updated online tool to compute cosmic-ray exposure ages. *Quaternary Geochronology*, 38: 25–49. doi: 10.1016/j.quageo.2016.11.006.

Milliman, J.D. & Farnsworth, K.L., 2013. *River Discharge to the Coastal Ocean: A Global Synthesis*. Cambridge University Press, UK.

Molina, A., Govers, G., Poesen, J., Van Hemelryck, H., De Bièvre, B. & Vanacker, V., 2008. Environmental factors controlling spatial variation in sediment yield in a central Andean mountain area. *Geomorphology*, 98(3–4): 176-186. doi: 10.1016/j.geomorph.2006.12.025.

Molina, A., Vanacker, V., Brisson, E., Mora, D. & Balthazar, V., 2015. Multidecadal change in streamflow associated with anthropogenic disturbances in the tropical Andes. *Hydrology and Earth System Sciences*, 19(10): 4201–4213. doi: 10.5194/hess-19-4201-2015.

Molina, A., Vanacker, V., Corre, M.D. & Veldkamp, E., 2019. Patterns in soil chemical weathering related to topographic gradients and vegetation structure in a high Andean tropical ecosystem. *Journal of Geophysical Research: Earth Surface*, 124(2): 666-685. doi: 10.1029/2018jf004856.

Montgomery, D.R., Dietrich, W.E. & Heffner, J.T., 2002. Piezometric response in shallow bedrock at CB1: Implications for runoff generation and landsliding. *Water Resources Research*, 38(12): 10–18. doi: 10.1029/2002WR001429.

Morera, S.B., Condom, T., Crave, A., Steer, P. & Guyot, J.L., 2017. The impact of extreme El Niño events on modern sediment transport along the western Peruvian Andes (1968-2012). *Scientific Reports*, 7(1): 11947. doi: 10.1038/s41598-017-12220-x.

Muenchow, J., Brenning, A. & Richter, M., 2012. Geomorphic process rates of landslides along a humidity gradient in the tropical Andes. *Geomorphology*, 139–140: 271–284. doi: 10.1016/j.geomorph.2011.10.029.

Niemi, N.A., Oskin, M., Burbank, D.W., Heimsath, A.M. & Gabet, E.J., 2005. Effects of bedrock landslides on cosmogenically determined erosion rates. *Earth and Planetary Science Letters*, 237(3–4): 480–498. doi: 10.1016/j.epsl.2005.07.009.

Norton, K.P. & Vanacker, V., 2009. Effects of terrain smoothing on topographic shielding correction factors for cosmogenic nuclide-derived estimates of basin-averaged denudation rates. *Earth Surface Processes and Landforms*, 34: 145-154. doi: 10.1002/esp.1700.

Norton, K.P., von Blanckenburg, F., DiBiase, R., Schlunegger, F. & Kubik, P.W., 2011. Cosmogenic ^{10}Be-derived denudation rates of the Eastern and Southern European Alps. *International Journal of Earth Sciences*, 100(5): 1163-1179. doi: 10.1007/s00531-010-0626-y.

Pepin, E., Carretier, S., Guyot, J.L. & Escobar, F., 2010. Specific suspended sediment yields of the Andean rivers of Chile and their relationship to climate, slope and vegetation. *Hydrological Sciences Journal*, 55(7): 1190–1205. doi: 10.1080/02626667.2010.512868.

Portenga, E.W. & Bierman, P.R., 2011. Understanding earth's eroding surface with ^{10}Be. *GSA Today*, 21(8): 4–10. doi: 10.1130/G111A.1.

Rosas, M.A., Vanacker, V., Viveen, W., Gutierrez, R. & Huggel, C., 2020. The potential impact of climate variability on siltation of Andean reservoirs. *Journal of Hydrology,* 581: 124396 doi: 10.1016/J.jhydrol.2019.124396.

Schuerch, P., Densmore, A.L., McArdell, B.W. & Molnar, P., 2006. The influence of landsliding on sediment supply and channel change in a steep mountain catchment. *Geomorphology*, 78(3–4): 222–235. doi: 10.1016/j.geomorph.2006.01.025.

Schwab, M., Rieke-Zapp, D., Schneider, H., Liniger, M. & Schlunegger, F., 2008. Landsliding and sediment flux in the Central Swiss Alps: A photogrammetric study of the Schimbrig landslide, Entlebuch. *Geomorphology*, 97(3–4): 392–406. doi: 10.1016/j.geomorph.2007.08.019.

Siame, L.L., Angelier, J., Chen, R.F., Godard, V., Derrieux, F, Bourles, D.L., Braucher, R., Chang, K.J., Chu, H.T., Lee, J.C., 2011. Erosion rates in an active orogen (NE-Taiwan): A confrontation of cosmogenic measurements with river suspended loads. *Quaternary Geochronology*, 6(2): 246–260. doi: 10.1016/j.quageo.2010.11.003.

Sidle, R.C., Ziegler, A.D., Negishi, J.N., Rahim Nik, A., Siew, R. & Turkelboom, F., 2006. Erosion processes in steep terrain - Truths, myths, and uncertainties related to forest management in Southeast Asia. *Forest Ecology and Management*, 224(1–2): 199–225. doi: 10.1016/j.foreco.2005.12.019.

Starke, J., Ehlers, T.A. & Schaller, M., 2017. Tectonic and Climatic Controls on the Spatial Distribution of Denudation Rates in Northern Chile (18°S to 23°S) Determined From Cosmogenic Nuclides. *Journal of Geophysical Research: Earth Surface*, 122(10): 1949–1971. doi: 10.1002/2016JF004153.

Tenorio, G.E., Vanacker, V., Campforts, B., Alvarez, L., Zhiminaicela, S., Vercruysse, K., Molina, A. & Govers, G., 2018. Tracking spatial variation in river load from Andean highlands to inter-Andean valleys. *Geomorphology*, 308: 175-189. doi: 10.1016/j.geomorph.2018.02.009.

Tobar, V. & Wyseure, G., 2018. Seasonal rainfall patterns classification, relationship to ENSO and rainfall trends in Ecuador. *International Journal of Climatology*, 38(4): 1808–1819. doi: 10.1002/joc.5297.

Tote, C., Govers, G., Van Kerckhoven, S., Filiberto, I., Verstraeten, G. & Eerens, H., 2011. Effect of ENSO events on sediment production in a large coastal basin in northern Peru. *Earth Surface Processes and Landforms*, 36(13): 1776–1788. doi: 10.1002/esp.2200.

Townsend-Small, A., McClain, M.E., Hall, B., Noguera, J.L., Llerena, C.A. & Brandes, J.A., 2008. Suspended sediments and organic matter in mountain headwaters of the Amazon River: Results from a 1-year time series study in the central Peruvian Andes. *Geochimica et Cosmochimica Acta*, 72(3): 732–740. doi: 10.1016/j.gca.2007.11.020.

von Blanckenburg, F., Belshaw, N. & O'Nions, R., 1996. Separation of ^{9}Be and cosmogenic ^{10}Be from environmental materials and SIMS isotope dilution analysis. *Chemical Geology*, 129: 93–99.

Vanacker, V., Vanderschaeghe, M., Govers, G., Willems, E., Poesen, J., Deckers, J. & De Bievre, B., 2003. Linking hydrological, infinite slope stability and land-use change models through GIS for assessing the impact of deforestation on slope stability in high Andean watersheds. *Geomorphology*, 52(3–4): 299–315. doi: 10.1016/S0169-555X(02)00263-5.

Vanacker, V., Molina, A., Govers, G., Poesen, J. & Deckers, J., 2007a. Spatial variation of suspended sediment concentrations in a tropical Andean river system: The Paute River, southern Ecuador. *Geomorphology*, 87(1–2): 53–67. doi: 10.1016/j.geomorph.2006.06.042.

Vanacker, V., von Blanckenburg, F., Govers, G., Molina, A., Poesen, J., Deckers, J. & Kubik, P.W., 2007b. Restoring dense vegetation can slow mountain erosion to near natural benchmark levels. *Geology*, 35(4): 303–306. doi: 10.1130/G23109A.1.

Vanacker, V., von Blanckenburg, F., Govers, G., Campforts, B., Molina, A., Kubik, P.W., 2015. Transient river response, captured by the channel steepness and it s concavity. *Geomorphology*, 228: 234–243. doi: 10.1016/j.geomorph.2014.09.013.

Vermeesch, P., 2007. CosmoCalc: An Excel add-in for cosmogenic nuclide calculations. *Geochemistry, Geophysics, Geosystems*, 8: Q08003. doi: 10.1029/2006GC001530.

Vicente-Serrano, S.M., Aguilar, E., Martinez, R., Martin-Hernandez, N., Azorin-Molina, C., Sanchez-Lorenzo, A., El Kenawy, A., Tomas-Burguera, M., Moran-Tejeda, E., Lopez-Moreno, J.I., Revuelto, J., Begueria, S., Nieto, J.J., Drumond, A., Gimeno, L. & Nieto, R., 2017. The complex influence of ENSO on droughts in Ecuador. *Climate Dynamics*, 48(1–2): 405–427. doi: 10.1007/s00382-016-3082-y.

Winter, T., Avouac, J.P. & Lavenu, A., 1993. Late Quaternary Kinematics of the Pallatanga Strike-Slip-Fault (Central Ecuador) from Topographic Measurements of Displaced Morphological Features. *Geophysical Journal International*, 115(3): 905–920. doi: 10.1111/j.1365-246X.1993.tb01500.x.

Yanites, B.J., Tucker, G.E. & Anderson, R.S., 2009. Numerical and analytical models of cosmogenic radionuclide dynamics in landslide-dominated drainage basins. *Journal of Geophysical Research: Earth Surface*, 114(1). doi: 10.1029/2008JF001088.